140 (2022) 213090

Contents lists available at ScienceDirect

Biomaterials Advances

journal homepage: www.journals.elsevier.com/materials-science-and-engineering-c

Magnetite and bismuth sulfide Janus heterostructures as radiosensitizers for *in vivo* enhanced radiotherapy in breast cancer

Hamed Nosrati [a], Mohammadreza Ghaffarlou [b], Marziyeh Salehiabar [c], Navid Mousazadeh [d], Fatemeh Abhari [d], Murat Barsbay [b], Yavuz Nuri Ertas [c,e], Hamid Rashidzadeh [c], Ali Mohammadi [d], Leila Nasehi [f], Hamed Rezaeejam [g], Soodabeh Davaran [h], Ali Ramazani [a,i,*], João Conde [j,**], Hossein Danafar [c,**]

[a] *Department of Biotechnology, Research Institute of Modern Biological Techniques (RIMBT), University of Zanjan, Zanjan 45371-38791, Iran*
[b] *Hacettepe University, Department of Chemistry, Beytepe, Ankara 06800, Turkey*
[c] *ERNAM—Nanotechnology Research and Application Center, Erciyes University, Kayseri 38039, Turkey*
[d] *Zanjan Pharmaceutical Biotechnology Research Center, Zanjan University of Medical Sciences, Zanjan, Iran*
[e] *Department of Biomedical Engineering, Erciyes University, Kayseri 38039, Turkey*
[f] *Department of Medical Laboratory, School of Paramedical Sciences, Zanjan University of Medical Sciences, Zanjan, Iran*
[g] *Department of Radiology, School of Paramedical Sciences, Zanjan University of Medical Sciences, Zanjan 45139-56184, Iran*
[h] *Drug Applied Research Center, Tabriz University of Medical Sciences, P.O. Box 51656-65811, Tabriz, Iran*
[i] *Department of Chemistry, Faculty of Science, University of Zanjan, Zanjan 45371-38791, Iran*
[j] *ToxOmics, NOVA Medical School|Faculdade de Ciências Médicas, NMS|FCM, Universidade Nova de Lisboa, 1169-056 Lisboa, Portugal*

ARTICLE INFO

Keywords:
Bismuth sulfide
Iron oxide
Janus nanoparticles
X-ray irradiation
Radiosensitizer
ROS generation

ABSTRACT

Janus heterostructures based on bimetallic nanoparticles have emerged as effective radiosensitizers owing to their radiosensitization capabilities in cancer cells. In this context, this study aims at developing a novel bimetallic nanoradiosensitizer, Bi_2S_3-Fe_3O_4, to enhance tumor accumulation and promote radiation-induced DNA damage while reducing adverse effects. Due to the presence of both iron oxide and bismuth sulfide metallic nanoparticles in these newly developed nanoparticle, strong radiosensitizing capacity is anticipated through the generation of reactive oxygen species (ROS) to induce DNA damage under X-Ray irradiation. To improve blood circulation time, biocompatibility, colloidal stability, and tuning surface functionalization, the surface of Bi_2S_3-Fe_3O_4 bimetallic nanoparticles was coated with bovine serum albumin (BSA). Moreover, to achieve higher cellular uptake and efficient tumor site specificity, folic acid (FA) as a targeting moiety was conjugated onto the bimetallic nanoparticles, termed Bi_2S_3@BSA-Fe_3O_4-FA. Biocompatibility, safety, radiation-induced DNA damage by ROS activation and generation, and radiosensitizing ability were confirmed *via in vitro* and *in vivo* assays. The administration of Bi_2S_3@BSA-Fe_3O_4-FA in 4T1 breast cancer murine model upon X-ray radiation revealed highly effective tumor eradication without causing any mortality or severe toxicity in healthy tissues. These findings offer compelling evidence for the potential capability of Bi_2S_3@BSA-Fe_3O_4-FA as an ideal nanoparticle for radiation-induced cancer therapy and open interesting avenues of future research in this area.

1. Introduction

Cancer is among the leading causes of morbidity and mortality worldwide, accounting for >10 million deaths in 2020 [1,2]. It is anticipated that the next decade is likely to witness a considerable rise in cancer incidence, morbidity and mortality globally [2,3]. Among the using of nanoparticle (NPs) for biological applications [4,5], there are a series of cancer therapy which harness nanoparticle for combatting cancer [6,7]. Radiation therapy (RT) as an efficient and palliative modality is employed for at least 50 % of all solid malignancies and extends the life expectancy of cancer patient through radiation-induced DNA damage of rapidly proliferating tumor cells [8]. In this context, ionizing

* Correspondence to: A. Ramazani, Department of Biotechnology, Research Institute of Modern Biological Techniques (RIMBT), University of Zanjan, Zanjan 45371-38791, Iran.
** Corresponding authors.
E-mail addresses: aliramazani@znu.ac.ir (A. Ramazani), joao.conde@nms.unl.pt (J. Conde), danafar@zums.ac.ir (H. Danafar).

https://doi.org/10.1016/j.bioadv.2022.213090
Received 7 July 2022; Received in revised form 17 August 2022; Accepted 20 August 2022
Available online 22 August 2022

radiation is used directly to treat tumor tissues or applied as a supplementary tool along with other common methods of cancer treatment. It has been well documented that to fully eradicate cancer cells and effectively shrink tumors, high doses of radiation are required, which may cause a serious risk of damage to neighboring healthy tissues, and this clinical problem has yet to be resolved [9]. Acute and/or late toxicity such as fibrosis, edema, and telangiectasia may occur in healthy tissues during radiation therapy and represent major obstacles for radiation dose escalation. Accordingly, effective radiation therapy has faced with the dilemma of how to maximally kill the tumor cells while not damaging the surrounding normal tissues. To address these, many research efforts have been conducted and among them, radiosensitizers have enormous potential in cancer radiotherapy [10]. These auspicious chemical or pharmacological agents make tumor cells more vulnerable to ionizing radiation by contributing to free radical formation and accelerating DNA damage through various mechanisms. Recent times have witnessed a rapid progress in the development of nanotechnology-based materials and advent of new medical technologies which provided promising nanoparticles for the rational design and development of radiation sensitizers characterized with low toxicity to the healthy tissues [11,12]. Nowadays, nanomaterial-based radiosensitizers have drawn great attention due to their excellent physicochemical features, including intrinsic radiosensitivity, high drug loading capacity, good biocompatibility, and effective tumor-targeting capability by enhanced permeability retention (EPR) effect [13,14]. Nanomaterial-based radiosensitizers can augment direct and indirect DNA damage upon radiation therapy, diminish radioresistance, and promote radioprotection of healthy tissues to accomplish successful radiation-induced cancer therapy [15]. Lately, in radiation-induced cancer therapy, high-Z materials have gained increased attention for their radiation dose-enhancement effect [16,17]. Nanomaterials comprising high-Z elements as potential radiosensitizers can absorb radiation and deposit the ionizing energy selectively and locally within tumors, then promote radiotherapy efficacy *via* radiation dose-enhancement effect. High-Z metallic nanoparticles, in particular bismuth sulfide nanoparticles (Bi_2S_3), are competent radiosensitizing agents with capability of augmenting the radiotherapy efficacy through several mechanisms [18,19]. In addition, over the past few years, bismuth as a biocompatible and inexpensive heavy metal element along with its derivatives such as Cu_3BiS_3 [20], Bi_2Se_3 [21], and Bi_2S_3@BSA [22,23] have been applied to cancer imaging and cancer radiotherapy. Bismuth sulfide nanoparticles (Bi_2S_3) owing to large X-ray attenuation coefficient (5.74 keV) and narrow direct bandgap (≈1.3 eV) of bismuth have been employed for X-ray computed tomography (CT) imaging and cancer radiotherapy [22,24,25].

Nosrati et al. prepared a heterostructure containing Bi_2S_3@BSA and gold nanoparticles, and evaluate their radiosensitizing ability *in vitro* and *in vivo* [23]. In another study, Huang et al. evaluated radioenhancing effect of dumbbell-shaped heterogeneous copper selenide-gold nanoparticles in murine model [26].

The advent of multifunctional nanosystems, along with advances in developing highly integrated bimetallic nanoparticles and rational design, would be a very promising strategy, due to the fact that, combined therapy offers superior performance over monotherapy in dealing with cancer [27]. Accordingly, there has been a shift of focus in clinical research from a single treatment modality to a combined therapy [23]. Generally, combination-based cancer therapy exhibits a better treatment outcome than the individual therapeutic agents, leading to dose reductions of prescription drugs [28].

It was found that the 50 nm-sized Au nanoparticles have a stronger radiosensitization effect than the 14 and 74 nm-sized ones because the 50 nm-sized gold nanoparticles have the highest cellular uptake [29].

There are studies in the literature on the radiosensitizing activities' of magnetic particles (like Fe_3O_4) [30] and semiconductor (like Bi2S3) nanoparticles [18]. However, there is no study investigating the radiosensitizing performance of "magnetic" Bi_2S_3 nanoparticles in cancer radiotherapy. The magnetic Bi_2S_3 synthesis attempts available in the literature have been carried out by solvothermal or hydrothermal synthesis approaches to date [31–34]. Apart from this novelty regarding the application, the synthesis method and structures of the nanoparticles obtained are also completely innovative compared to those in the literature.

None of the magnetic bismuth particles obtained in these high-temperature syntheses are Janus nanoparticles with promising heterojunctions, and moreover, they are "micron" in size.

In this regard, we developed an effective heterostructured radiosensitizer based on Bi_2S_3 and Fe_3O_4 nanoparticles to induce radiation therapy effect. However, in the current work, we present the Janus-type magnetic Bi_2S_3 "nano"particle formation for the first time. Moreover, we do this by being inspired by nature. The synthesis of the Janus nanoparticles were carried out in a very similar way to the biomineralization process of living organisms, where selective interactions with inorganic ions are involved and scaffolds for minerals are provided, mostly through functional proteins. Without any additional modification, the resulting Janus nanoparticles were also stabilized by BSA and exhibited high biocompatibility and targeting ability thanks to their envelop. Janus nanoparticles obtained by this method have promising heterojunctions, in addition to being completely nanosized and uniformly distributed.

Due to the presence of both iron oxide and bismuth sulfide nanoparticle in the structure, great tumor radiosensitivity is expected through reactive oxygen species (ROS) generation and DNA damage. To improve the targeting specificity, folic acid (FA) was covalently conjugated onto the Bi_2S_3@BSA-Fe_3O_4 nanoparticles (Fig. 1). Bi_2S_3@BSA-Fe_3O_4–FA nanoradiosensitizers not only make tumor cells more prone to radiation-induced damage, but also exert a high targeting capability due to the presence of FA. By a single dose injection of the bimetallic nanoparticles, a strong anticancer effect was observed under X-Ray irradiation.

2. Materials and methods

2.1. Materials

$Bi_2(NO_3)_3$. $5H_2O$, BSA, FA, 1-ethyl-3-(3-(dimethylamine)-propyl) carbodiimide (EDC), N-hydroxysuccinimide (NHS), 3-(4,5-dimethylthiazol-2-yl)-2,5-diphenyltetrazolium bromide (MTT), fluorescein isothiocyanate (FITC), 2,7-dichlorodihydrofluorescein diacetate (DCFH-DA), Calcein-AM and Propidium Iodide (PI), and crystal violet were purchased from Sigma-Aldrich (St. Louis, USA). $FeCl_2.4H_2O$, $FeCl_3.6H_2O$, and NH_4OH were purchased from Merck (Kenilworth, USA).

2.2. Methods

2.2.1. Synthesis of BSA coated bismuth sulfide nanoparticles (Bi_2S_3@BSA)

Bismuth nitrate solution with a portion of $Bi(NO_3)_3$ (50 mM) in 1 mL nitric acid (2 M) was gradually added to 8 mL of BSA solution (31.25 mg/ mL) under vigorous stirring. After the complex of BSA and Bi was formed, by simply adding of $NaOH_{(aq)}$ to the formed complex solution (Bi-BSA) and stirring for 12 h, the colorless solution was changed to black color, and the BSA coated bismuth sulfide nanoparticles were formed through biomineralization process. The resulting product was then dialyzed against distilled water for 48 h to obtain the impurity-free Bi_2S_3@BSA nanoparticles.

2.2.2. Synthesis of iron oxide–bismuth sulfide bimetallic nanoparticles (Bi_2S_3@BSA-Fe_3O_4)

For the preparation of Bi_2S_3@BSA-Fe_3O_4 hybrid nanoparticles, Fe_3O_4 nanoparticles were synthesized in the presence of pre-obtained Bi_2S_3@BSA nanoparticles. In brief, a known amount of NH_4OH was introduced dropwise to an aqueous solution containing 40.0 mg

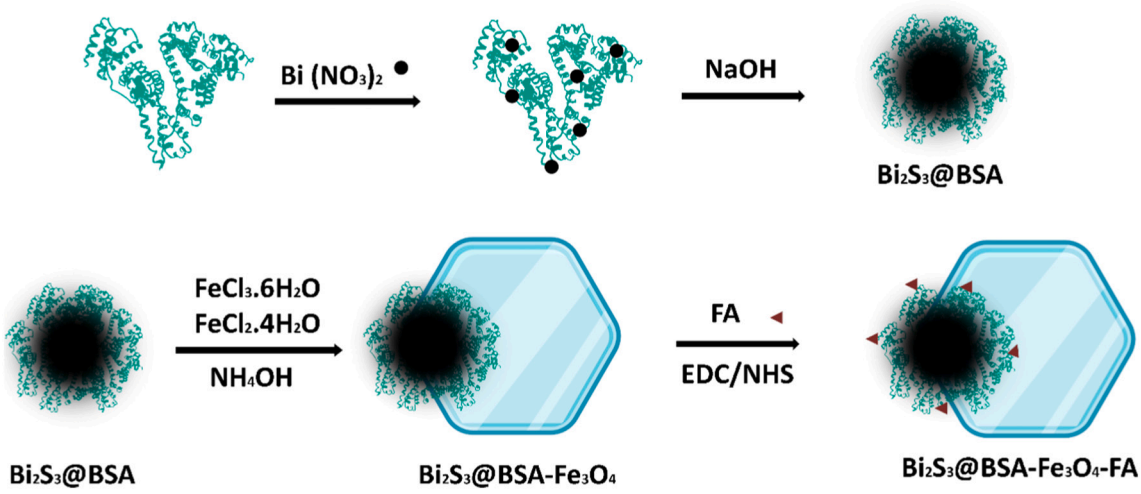

Fig. 1. (a) Schematic representation of the three steps in preparation of Bi_2S_3@BSA-Fe_3O_4-FA nanoradiosensitizers.

$FeCl_2.4H_2O$, 110.0 mg $FeCl_3.6H_2O$ and 500 mg of pre-synthesized Bi_2S_3@BSA nanoparticles under vigorous stirring in N_2 atmosphere and heating at 60 °C. The reaction mixture was stirred for 12 h and the resulting product, Bi_2S_3@BSA-Fe_3O_4, were then dialyzed against distilled water for 48 h to obtain the impurity-free Bi_2S_3@BSA-Fe_3O_4 nanoparticles.

2.2.3. Preparation of folic acid conjugated nanoparticles (Bi_2S_3@BSA-Fe_3O_4-FA)

To achieve higher cellular uptake as well as efficient tumor site specificity, folic acid (FA) as a targeting moiety was conjugated to the bimetallic nanoparticles. In this context, the carboxylic acid groups of FA were first activated by EDC and NHS. In brief, 31.6 mg EDC and 20.0 mg of NHS along with 15.0 mg FA were mixed in 1.0 mL dimethylsulfoxide (DMSO). Then, this mixture was gradually added to the aqueous solution containing 150.0 mg of bimetallic Bi_2S_3@BSA-Fe_3O_4 nanoparticles. NaOH solution (3.0 M) was also used to maintain the pH value at 8.2, and the reaction was stirred for 24 h. The resulting product was dialyzed against distilled water for 48 h to obtain the impurity-free Bi_2S_3@BSA-Fe_3O_4-FA nanoparticles.

2.2.4. Bi_2S_3@BSA-Fe_3O_4-FA characterization

Several characterization techniques were used to determine and analyze the synthesized hybrid structure. Field emission scanning electron microscopy and X-ray mapping (FESEM, ZEISS, GEMINI 500), scanning transmission electron microscope (STEM, ZEISS, GEMINI 500), transmission electron microscopy and X-ray mapping (TEM, FEI 120 kV) were applied to characterize the structure and morphology of the prepared nanoparticles. Energy dispersive spectroscopy (EDS) is generally used to qualitatively determine the amount of the main elements and produce elemental distribution maps. To obtain XRD patterns, a powder X-ray diffractometer system (PANalytical X'Pert Powder Diffractometer) was used. A mono-chromatized Al Ka X-ray source (Thermo Scientific) was employed for X-Ray photoelectron studies. UV–vis absorption spectra was acquired by a UV/Vis spectrophotometer (T80 double beam spectrophotometer, PG Instruments Limited). Fourier-transform infrared (FTIR) spectra were documented by FTIR spectroscopy (FTIR; SHIMADZU, Model IRTRACER-100). Both mean particle size and hydrodynamic size distribution as well as zeta potential of developed hybrid system were determined by using dynamic light scattering (DLS) on a nano/zetasizer (Malvern Instruments, Worcestershire, UK, ZEN 3600 model Nano ZS).

2.2.5. Determination of the FA conjugation amount onto Bi_2S_3@BSA-Fe_3O_4

To determine the amount of covalently bound FA moieties on the surface of Bi_2S_3@BSA-Fe_3O_4 nanoparticles, UV–Vis spectrophotometer was employed. In brief, 0.50 mg Bi_2S_3@BSA-Fe_3O_4-FA along with 0.50 mg proteinase K enzyme were dispersed in 1.0 mL of PBS:Ethanol (70:30) (pH: 7.4). Then, this mixture was incubated overnight at 37 °C with gentle shaking. After completion of the incubation period, the mixture was centrifuged for 10 min at 13,000 rpm, and the absorbance of the supernatant containing FA was determined by a UV–Vis spectrophotometer at 352 nm.

2.2.6. In vitro assays

2.2.6.1. Analysis of hemocompatibility. Human erythrocytes were collected and washed with sterile PBS (pH: 7.4). Then, 0.5 mL of erythrocyte suspension was introduced to vials containing Bi_2S_3@BSA, Bi_2S_3@BSA-Fe_3O_4 and Bi_2S_3@BSA-Fe_3O_4-FA with different concentrations (25, 75 and 225 mg/mL). Deionized water and PBS were used as positive and negative controls, respectively. Next, the suspension was incubated at 37 °C for 4 h with gentle shaking. After completion of the incubation period, the suspension containing erythrocytes and nanoparticles was centrifuged for 15 min at 13,000 rpm, the absorbance of the supernatant containing hemoglobin was determined by a UV–Vis spectrophotometer at 540 nm, and the hemolysis value was determined using the following equation (Eq. (2)):

$$\%\text{Hemolysis} = \frac{A\ (sample) - A\ (negative)}{A\ (positive) - A\ (negative)} \times 100 \quad (1)$$

Hemolysis assay for each concentration was carried out in triplicates (n = 3).

2.2.6.2. Analysis of cytotoxicity against healthy cells. *In vitro* cytotoxicity assay was conducted to reveal that cytotoxic effects of the prepared nanoparticles on healthy cells (HFF-2 cells). Accordingly, once HFF-2 cells reached to the desired confluency and density, they were seeded in a 96-well plate at a density of 5×10^3 cells per well and incubated for 24 h. Then, the medium was discarded and new media containing 25, 75 and 225 mg mL of Bi_2S_3@BSA-Fe_3O_4-FA was introduced to the each well. After incubation for 5 h, the medium was removed and replaced with fresh medium and incubated for an additional 24 h. After that, MTT solution (20 μL with concentration of 5 mg/mL) was added to each well. The purple formazan crystals are formed during the incubation period of 4 h, and after removing media, DMSO (100 mL per well) was added to dissolve these insoluble crystals. The optical density (OD) was recorded

using a microplate reader (Bio-Tek, USA) at 570 nm. This analysis was performed in quintuplicates (n = 5).

2.2.6.3. In vitro anti-cancer activity. Cytotoxicity potential of Bi_2S_3@BSA, Bi_2S_3@BSA-Fe_3O_4 and Bi_2S_3@BSA-Fe_3O_4-FA nanoparticles was investigated against the mouse breast carcinoma cell line (4T1 cells). Similarly, this assay was performed by MTT test according to the above-mentioned protocols but in the presence and absence of X-ray irradiation. Briefly, after 4T1 cells were seeded and incubated in a 96-well plate (5×10^3 cells per well), they were treated with Bi_2S_3@BSA, Bi_2S_3@BSA-Fe_3O_4 and Bi_2S_3@BSA-Fe_3O_4-FA with different concentrations (25, 75 and 225 mg / mL). Wells with no treatment were considered as negative controls. After 5 h of incubation, the medium containing nanoparticles was removed and the wells were washed with PBS, and then fresh medium was then added. In this step, cells were exposed to X-ray (4 Gy, 6 MV) followed by incubation for 24 h. Finally, as previously explained in the above section, MTT assay was used to ascertain the efficacy of the developed nanoparticles against 4T1 cells upon X-ray radiation. Of note, MTT assay was also performed without X-ray radiation to evaluate whether the radiotherapy is effective or not in reducing the cell viability of cancer cells.

2.2.6.4. Cellular uptake and internalization efficacy. Both Bi_2S_3@BSA-Fe_3O_4 and Bi_2S_3@BSA-Fe_3O_4-FA nanoparticles were labeled with FITC to determine whether the conjugation of FA was effective in enhancing the cellular uptake and targeting capability of developed nanoparticles. In this context, 4T1 cells were seeded in a 24-well plate at a density of 1.5×10^5 cells per well. After the confluency of cells reached to the desired amount (80 %), they were co-incubated with as prepared FITC-labeled nanoparticles (50 μg/mL) for 5 h. Cells were then washed to remove any impurities such as debris prior to analysis by flow cytometer (BD Biosciences, San Jose, CA).

2.2.6.5. Intracellular ROS generation. 4T1 cells were seeded in a 96-well culture plate at a density of 5×10^5 cells per well and incubated overnight. Then, cells were co-incubated with different treatment groups including Bi_2S_3@BSA, Bi_2S_3@BSA-Fe_3O_4 and Bi_2S_3@BSA-Fe_3O_4-FA for 5 h. Next, cells were washed and incubated for further 1 h in RPMI-1640 medium containing 10 μM DCFH-DA. Finally, the cells were exposed to X-ray radiation (4 Gy, 6 MV), visualized by a fluorescence microscope, and assessed using ImageJ software.

2.2.6.6. Calcein AM/PI cell staining assay. Nanoradiosensitizer-triggered death of 4T1 cells upon X-ray irradiation was exploited *via* Calcein AM/PI staining method. In brief, 4T1 cells were seeded in a 8-well chamber slide (3×10^5 cell per well) and incubated for 24 h, then it was subjected to various treatment groups including control, X-ray, Bi_2S_3@BSA + X-ray, Bi_2S_3@BSA-Fe_3O_4 + X-ray and Bi_2S_3@BSA-Fe_3O_4-FA + X-ray for another 24 h. Afterwards, Calcein AM (3 μM) was added and incubated for 30 min followed by incubation with PI (4 μM) for 5 min. Eventually, green (live) and red (dead) fluorescence images of 4T1 cells were observed.

2.2.6.7. Apoptosis assay. Apoptosis is a favorable process in cancer radiotherapy, and it can be enhanced by nanoparticles. Apoptosis assay was performed according to the previously reported protocol [30].

2.2.6.8. Clonogenic assay. In order to evaluate the radiosensitizing capacity of developed Bi_2S_3@BSA, Bi_2S_3@BSA-Fe_3O_4 and Bi_2S_3@BSA-Fe_3O_4-FA nanoparticles in the presence of X-ray irradiation, the clonogenic assay was performed according to the previously reported method [35].

2.2.7. In vivo assays

2.2.7.1. LD_{50} analysis as an in vivo safety indicator. LD_{50} test was performed using BALB/c female mice (~20 g weight). Bi_2S_3@BSA-Fe_3O_4-FA nanoparticles with different concentrations of 0, 50, 150 and 450 mg/kg were administrated to mice by intravenous injection. To determine the $LD_{50,}$ mice were then monitored for any changes in their body weight and survival rate for three weeks. Each test was performed in quadruplicates (n = 4 mice per dose).

2.2.7.2. In vivo antitumor activity. In vivo antitumor activity of Bi_2S_3@BSA, Bi_2S_3@BSA-Fe_3O_4 and Bi_2S_3@BSA-Fe_3O_4-FA nanoparticles was investigated against the mouse breast cancer model in the presence and absence of X-ray radiation. Murine breast tumor model was established by subcutaneous injection of 1×10^6 4T1 cells into the right flank of BALB/c female mice. After two weeks of inoculation, the tumor volume was determined by means of a digital caliper in two directions of length (L) and width (W) using the following formula: $V = 0.5 \times L \times W^2$. To initiate the assessment, tumor volumes must reach to the volume of 100 mm^3, and once this has reached the mice were randomly divided into six groups (N = 7). Randomized mice groups were then treated with different regimens as follows: (1) Bi_2S_3@BSA-Fe_3O_4-FA, (2) Bi_2S_3@BSA-Fe_3O_4-FA with 4Gy X-ray, (3) Bi_2S_3@BSA-Fe_3O_4 with 4Gy X-ray, (4) Bi_2S_3@BSA with 4Gy X-ray, (5) PBS and (6) X-ray. Of note, all the aforementioned materials were intravenously injected into the mice through the tail vein. Then, both body weight and tumor volume of each mouse were precisely monitored during the experimental time periods.

2.3. Histopathology analysis

To investigate tumor histopathology, on the second day of treatment, and also for histopathology study of the key organs of mice such as the kidney, spleen, liver and heart, on the 15th day of treatment, mice from different groups were euthanized, their organs were collected, fixed in 4 % paraformaldehyde, embedded in paraffin and sectioned at a thickness of 5 mm. All sections were stained with hematoxylin and eosin (H&E) prior to microscopic analysis.

2.4. Statistical analysis

All of the quantitative data were expressed as mean with standard deviation (mean ± SD) unless otherwise stated. Statistical analysis was performed using GraphPad Prism software (GraphPad Prism 8).

3. Results and discussion

3.1. Synthesis procedure of Bi_2S_3@BSA-Fe_3O_4-FA nanoradiosensitizers

Synthesis of Bi_2S_3@BSA-Fe_3O_4-FA nanoradiosensitizers was conducted by following steps. I) Synthesis of Bi_2S_3@BSA: The preparation of BSA@Bi_2S_3 nanoparticles is very similar to the biomineralization process of living organisms, where selective interactions with inorganic ions are involved and scaffolds for minerals are provided, mostly through functional proteins [36,37]. After adding Bi^{3+} ions to the aqueous BSA solution, the protein molecules sequester and trap Bi^{3+} to form BSA-Bi^{3+} complexes. By adjusting the pH to 12.00, BSA denatures to release residues such as 35 cysteine, an excellent source of sulfur, which leads to the formation of Bi_2S_3 [37]. During this biomineralization process, Bi_2S_3 nanoparticles are covered with BSA, making them highly stable, biocompatible, and suitable for further modifications. Preparation of the hybrid bimetallic Bi_2S_3@BSA-Fe_3O_4 nanoparticles: For the preparation of the dual hybrid nanoparticles, Fe_3O_4 nanoparticles were synthesized *via* co-precipitation method using $FeCl_2.4H_2O$ and $FeCl_3.6H_2O$. During their formation in the presence of pre-synthesized Bi_2S_3@BSA, Fe_3O_4 nanoparticles were stabilized by BSA and added as a new component to

the hybrid nanoparticle structure. Preparation of Bi_2S_3@BSA-Fe_3O_4-FA nanoradiosensitizers: This process was accomplished by activating the carboxylic acid groups of FA using EDC and NHS, followed by the reaction of amine groups of Bi_2S_3@BSA with carboxylic acid groups of FA to form amide bonds. Schematic representation of all these three steps of Bi_2S_3@BSA-Fe_3O_4-FA nanoradiosensitizer synthesis is shown in Fig. 1a. EDS survey scans (Fig. S1b) further confirmed the synthesis of each nanostructure. The full-range spectrum of Bi_2S_3@BSA-Fe_3O_4-FA nanoradiosensitizers showed the presence of each element in the structure. SEM-EDS-mapping was used to confirm the presence of Fe and Bi metals in bimetallic nanoparticles. The EDS mapping images of Bi, S, C, N, O, and Fe confirmed the presence of all these elements in the final formulation (Fig. 1c). UV–Vis spectrophotometry analysis was applied to determine the amount of FA conjugated to the surface of Bi_2S_3@BSA-Fe_3O_4. The amount of conjugated FA was found to be 8.81 μg per 100 μg of the final formulation. The cellular uptake and targeting capability of the designed nanoparticles are expected to be significantly enhanced by FA conjugation compared to non-targeted nanoparticles [38–40]. It was recently reported that PNIPAM-*co*-PβCD@FA nanostructured copolymer brushes could effectively kill cancer cells compared to the non-targeted copolymer [41].

3.2. Bi_2S_3@BSA-Fe_3O_4-FA nanoradiosensitizers characterization

Different characterization techniques were used to elucidate the morphology and structure of the as-prepared bimetallic nanoparticles. The size and morphology of Bi_2S_3@BSA and Bi_2S_3@BSA-Fe_3O_4 nanoparticles were investigated by TEM. Before the incorporation of Fe_3O_4 NPs into the heterodimer structure, Bi_2S_3@BSA nanoparticles are in spherical shape with a diameter of approximately 5–25 nm (Fig. 2a). Spherical and polygonal Fe_3O_4 nanoparticles display lighter contrast compared to Bi_2S_3 in the TEM image of Bi_2S_3@BSA-Fe_3O_4 dual hybrid nanoparticles (Fig. 2a, b, c). For Fe_3O_4 NPs obtained by co-precipitation, polygonal geometries have been reported previously [42,43]. The contrast that nanoparticles will exhibit in TEM analysis is closely related to their electron densities. Since bismuth (Bi) has a higher electron density than Fe_3O_4, Bi_2S_3 appears darker than Fe_3O_4 in TEM images as lower electron density of Fe allows more electrons to be transmitted.

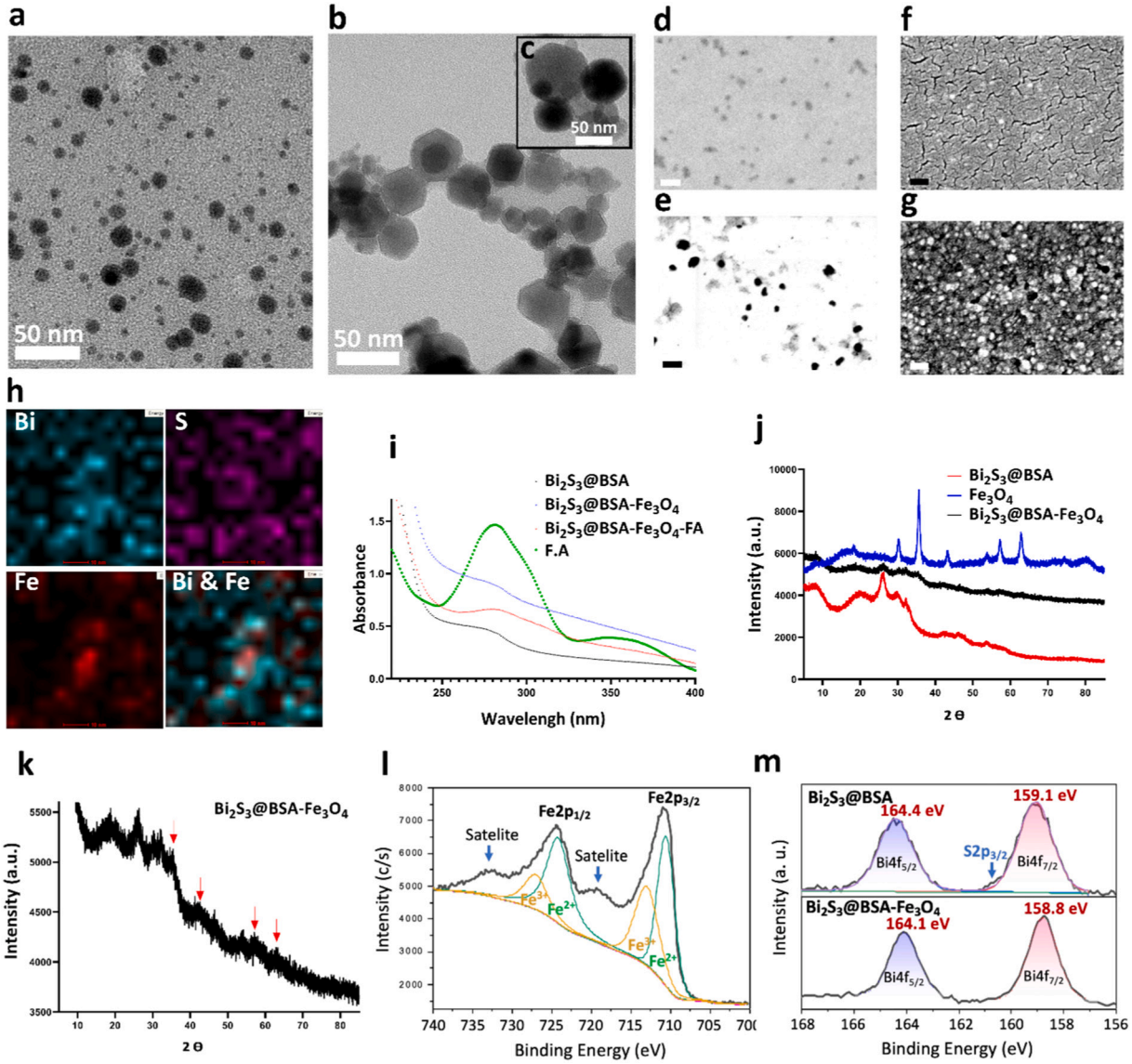

Fig. 2. Characterization: TEM image of (a) Bi_2S_3@BSA and (b, c) Bi_2S_3@BSA-Fe_3O_4; STEM image of (d) Bi_2S_3@BSA and (e) Bi_2S_3@BSA-Fe_3O_4; FESEM image of (f) Bi_2S_3@BSA and (g) Bi_2S_3@BSA-Fe_3O_4 (scale bar for STEM images is 50 nm); (h) TEM-EDS mapping analysis of Bi_2S_3@BSA-Fe_3O_4; (i) UV–Vis spectra of Bi_2S_3@BSA, Bi_2S_3@BSA-Fe_3O_4, Bi_2S_3@BSA-Fe_3O_4-FA, and FA; (j) XRD patterns of Bi_2S_3@BSA, Fe_3O_4, and Bi_2S_3@BSA-Fe_3O_4 (k) Expanded XRD pattern of Bi_2S_3@BSA-Fe_3O_4; (l) Fe2p core-level XPS spectrum of Bi_2S_3@BSA-Fe_3O_4; (m) Bi4f core-level XPS spectra of Bi_2S_3@BSA (top spectrum) and Bi_2S_3@BSA-Fe_3O_4 (bottom spectrum).

Also, BSA is clearly visible in Fig. 2d as a thin organic layer covering the surface of the heterodimers. This figure is notable such that it shows Bi_2S_3 and Fe_3O_4 nanoparticles with dark and light contrasts, respectively. After the addition of Fe_3O_4 to Bi_2S_3@BSA nanoparticles, mean particle size gradually increased which was validated by TEM and STEM imaging (Fig. 2b, c, e). FESEM analysis (Fig. 2g) highlights uniform nanoparticle size distributions and increase in nanoparticle sizes after the formation of Bi_2S_3@BSA-Fe_3O_4 heterodimer, compared to Bi_2S_3@BSA (Fig. 2d and f). EDS-mapping was used to confirm the presence of Fe and Bi metals in bimetallic hybrids. TEM-EDS mapping analysis of Bi_2S_3@BSA-Fe_3O_4 is shown in Fig. 2h, where the EDS mapping of Bi, S and Fe is represented, and the results confirmed the presence of all these elements in the final nanoformulation. UV–Vis spectrophotometer was also applied to study possible interactions of different components of the bimetallic hybrids as well as to confirm successful synthesis of the Bi_2S_3@BSA-Fe_3O_4-FA nanoparticles. UV–Vis spectra of FA, Bi_2S_3@BSA, Bi_2S_3@BSA-Fe_3O_4, and Bi_2S_3@BSA-Fe_3O_4-FA are shown in Fig. 2i, where the main absorbance peak of BSA in Bi_2S_3@BSA nanoparticles is clearly assigned at 263 nm. BSA-related absorbance peaks in Bi_2S_3@BSA-Fe_3O_4-FA exhibit a shift to higher wavelengths (redshift) compared to Bi_2S_3@BSA nanoparticles. Pure folic acid displayed two absorption peaks at 283 nm and 352 nm, where the former peak was observed in Bi_2S_3@BSA-Fe_3O_4-FA as well with a slight shift at 284 nm. These results confirmed the presence of BSA and FA in the structure of final formulation and thus the successful synthesis of Bi_2S_3@BSA-Fe_3O_4-FA nanoradiosensitizers.

In FT-IR spectrum (Fig. S2) of Bi2S3@BSA Characteristics peaks of BSA, amid I and amid II, appeared in at 1646 cm^{-1} and 1532 cm^{-1}, respectively. Strong peak at 1392 cm^{-1} was due to C—N bending vibration and the broad band around 660 and 601 cm^{-1} are attributed to Bi vibration [44,45]. In Bi_2S_3@BSA-Fe_3O_4 spectrum, peak positions at 1634 cm^{-1} and 1525 cm^{-1} (with a slight blue shift) matches well with Bi_2S_3@BSA. Moreover absorption peak at 531 cm^{-1}, which is in consistence with previous study, represents F—O bond indicating Fe_3O_4 existence and thus successful dual hybrid formation [46].

XRD is another technique for the characterization of Bi_2S_3@BSA-Fe_3O_4-FA nanoradiosensitizers. This technique is a frequently used tool in the characterization of nanoparticles, especially because of its speed and simplicity. Besides, XRD can provide useful information regarding the crystalline grain size, lattice parameters, nature of the phase and crystalline structure [47]. Accordingly, the latter parameter was exploited for the bare Fe_3O_4, Bi_2S_3@BSA and Bi_2S_3@BSA-Fe_3O_4-FA nanoparticles. The metallic character of iron and bismuth in Fe_3O_4 (JCPDS 019-0629) and Bi_2S_3@BSA (JCPDS 17-0320) nanoparticles, respectively, was verified by the JCPDS database (Fig. 2j). The XRD pattern of Bi_2S_3@BSA-Fe_3O_4 nanoparticles exhibited the characteristic peaks of both Fe and Bi, confirming the successful synthesis of bimetallic nanoradiosensitizers (Fig. 2k). X-ray photoelectron spectroscopy (XPS) is a common approach to determine the electronic structure and chemical states of materials through shifts in core-level binding energies induced by the immediate chemical environment of an atom. The core-level Fe2p spectrum of Bi_2S_3@BSA-Fe_3O_4 heterodimer, consisting of the doublet corresponding to $Fe2p_{3/2}$ and $Fe2p_{1/2}$, is shown in Fig. 2l. Fe_3O_4 contains both Fe^{2+} and Fe^{3+} ions. The Fe2p doublet is well-deconvoluted into four peaks corresponding to Fe^{2+} (710.6, 724.2 eV) and Fe^{3+} (713.1, 727.1 eV) ions in the Fe_3O_4 phase and is in a very good agreement with the standard Fe_3O_4 XPS spectrum [48–50]. The $Fe2p_{3/2}$ and $Fe2p_{1/2}$ spin orbit peaks are accompanied by their satellites at around 719.2 eV and 732.7 eV, respectively. These satellites are commonly regarded as the characteristics of γ-Fe_2O_3 phase [48,49]. It is noteworthy to observe these satellites to distinguish between Fe_3O_4 (magnetite) and γ-Fe_2O_3 (maghemite), because the two have the same crystal structure but differ only in the valence state of the iron ions [49]. The core-level Fe2p spectrum of Bi_2S_3@BSA-Fe_3O_4 therefore clearly confirms Fe_3O_4 as the main phase, while showing that some γ-Fe_2O_3 phase accompanies the structure (Fig. 2l). The Bi 4f core-level XPS spectrum of Bi_2S_3@BSA (upper spectrum, Fig. 2m) shows a spin–orbit doublet centered at 159.1 eV and 164.4 eV, which are assigned to $Bi4f_{7/2}$ and $Bi4f_{5/2}$ peaks, respectively. The $S2p_{1/2}$ spin–orbit peak of S2p doublet overlaps with the $Bi4f_{5/2}$ peak, while the $S2p_{3/2}$ component appears as a separate slight peak at 160.7 eV [51]. These assignments are consistent with previous reports on Bi_2S_3 crystals [23,51,52]. The core-level binding energies measured by XPS for nanostructures are not determined solely by the chemical environment of the atoms of interest. Additionally, electrostatic energy changes play an equivalently important role. Peak shifts of several tens of electron-volts can be caused by the rearrangement of interfacial charges or changes in the polarities of the structures under study [53]. As shown in Fig. 2m (lower spectrum), the Bi4f spin orbit doublet peaks become narrower, and both shift to a lower binding energy of approximately 0.3 eV once the Bi_2S_3-Fe_3O_4 heterodimers are formed. This is attributed to the changes in the electrostatic interactions at the heterojunctions of the Bi_2S_3 and Fe_3O_4 nanoparticles, indicating the formation of the heterodimer structure.

Hydrodynamic size of nanoparticles has a great impact on their biological applications; therefore, determination of this key feature is essential prior to *in vitro* and *in vivo* investigation. Accordingly, the hydrodynamic diameter of the final formulation was determined by DLS method. The mean hydrodynamic size of Bi_2S_3@BSA, Bi_2S_3@BSA-Fe_3O_4, and Bi_2S_3@BSA-Fe_3O_4-FA nanoparticles were 57, 71 and 86 nm, respectively (Fig. S3a). The size obtained by DLS measurement differs from that of it by SEM and TEM, which may be attributed to the fact that particles undergo hydration in DLS method (Fig. 2d-g). Finally, the size of final formulation (Bi_2S_3@BSA-Fe_3O_4-FA) was monitored for 30 days to further evaluate its potential stability (Fig. S3b). It was found that, there was no significant change in the size of Bi_2S_3@BSA-Fe_3O_4-FA formulation for over one month.

3.3. *In vitro assays*

3.3.1. *Analysis of hemocompatibility*

In order to achieve desired therapeutic effects, nanoparticles must enter the bloodstream, where they come into direct contact with blood components (platelets, proteins, white cells, red cells, *etc.*). Therefore, hemocompatibility is a major criterion for the clinical applicability of blood-contacting nanomaterials. Accordingly, blood compatibility of the developed Bi_2S_3@BSA, Bi_2S_3@BSA-Fe_3O_4 and Bi_2S_3@BSA-Fe_3O_4-FA nanoparticles was investigated against human red blood cells (HRBCs). The degree of hemolysis caused by these nanoparticles revealed that Bi_2S_3@BSA, Bi_2S_3@BSA-Fe_3O_4 and Bi_2S_3@BSA-Fe_3O_4-FA nanoparticles did not cause severe hemolysis even at high nanoparticle concentrations (Fig. 3a). Although the hemolytic effects of Bi_2S_3@BSA, Bi_2S_3@BSA-Fe_3O_4 and Bi_2S_3@BSA-Fe_3O_4-FA nanoparticles were concentration-dependent, their hemolysis activity did not exceed 5 % even at the maximum concentration of nanoparticles. These findings demonstrate that the novel bimetallic nanoparticles are practically nontoxic (hemolysis <5 %), and this is well supported by previously published data [54]. These results offer unprecedented evidence for the safe clinical application of the prepared bimetallic nanoradiosensitizers.

3.3.2. *Analysis of cytotoxicity against healthy cells*

Cytotoxicity assay is carried out to ascertain the cytotoxic potential of nanoparticles or other synthetic agents at the preclinical level and provides cell death rate against various doses of fabricated agents. Verification of toxicity potential of nanosystems on healthy cells is one of the required tests prior to determining their anticancer efficacy *in vitro*. Accordingly, HFF-2 cells as a normal cell line were incubated with different concentrations of Bi_2S_3@BSA-Fe_3O_4-FA ranging from 25 to 225 mg/mL. The MTT assay revealed that Bi_2S_3@BSA-Fe_3O_4-FA at all treated doses (25–225 mg/mL) had no adverse effect on survival rate of HFF-2 cells, underlining the biosafety of the synthesized nanoparticles (Fig. 3b). The cell viability was close to 100 % even at the concentration of 225 mg/mL (the highest concentration tested). These findings are

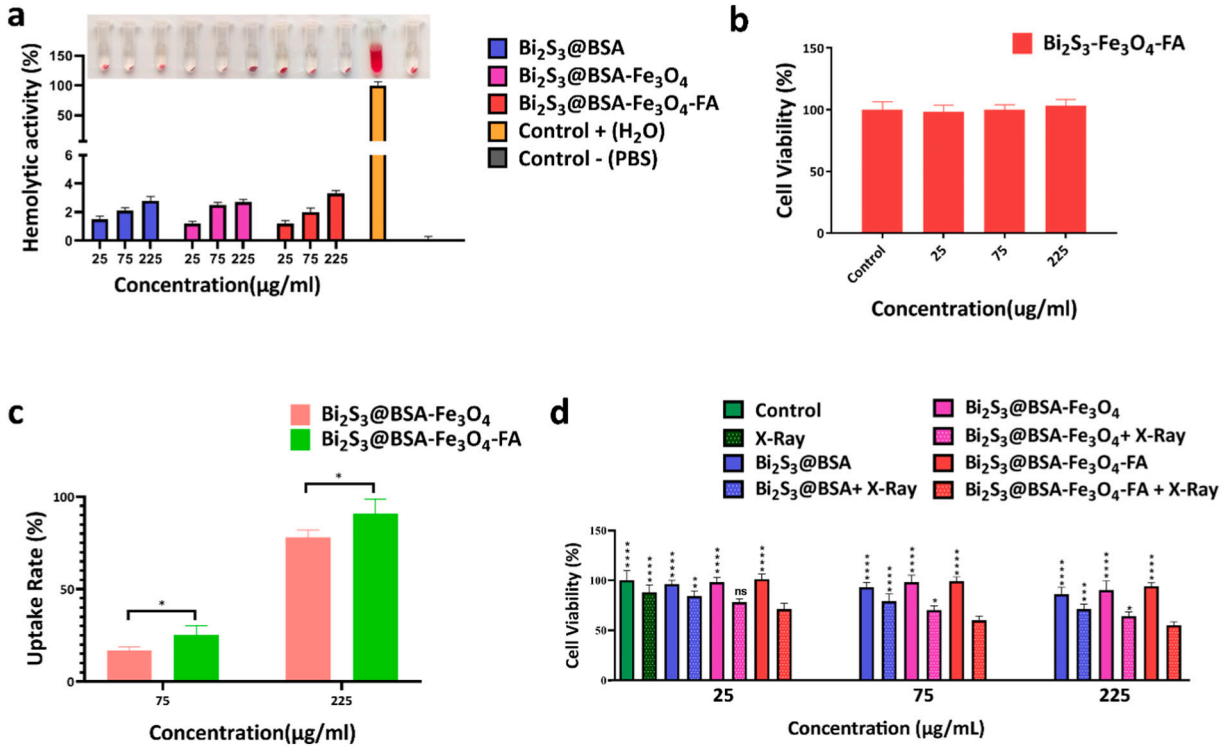

Fig. 3. *In vitro* assays: (a) Hemolytic activity of different nanoparticles; (b) cytotoxicity assay of Bi_2S_3@BSA-Fe_3O_4-FA on healthy cells; (c) cellular uptake of Bi_2S_3@BSA-Fe_3O_4 and Bi_2S_3@BSA-Fe_3O_4-FA nanoparticles. (c) *In vitro* studies of antitumor effects on 4T1 cells for various samples with or without X-ray irradiation.

consistent with those reported by other researchers, for instance, amino acid-coated magnetic nanoparticles exhibited no potential cytotoxicity against HFF-2 cells over a wide concentration range [55].

3.3.3. *In vitro anti-cancer activity*

After establishing the excellent biosafety, biocompatibility and hemocompatibility of nanoparticles developed through hemolysis test and MTT assay, we then evaluated the radiosensitization effect and anticancer activity by *in vitro* cell growth inhibition assay. The therapeutic effect of the nanoparticles in the presence and absence of X-ray irradiation at three different concentration (25, 75 and 225 mg/mL) were fully elucidated. The radiosensitizing capacities of Bi_2S_3@BSA, Bi_2S_3@BSA-Fe_3O_4 and Bi_2S_3@BSA-Fe_3O_4-FA nanoparticles against the mouse breast carcinoma cell line (4T1 cells) are shown in Fig. 3c. The results showed that X-ray radiation at a dose of 4 Gy slightly reduced cell viability, decreasing cell survival rate to 88 %, which underlines the importance of X-ray radiation (4 Gy), yet it did not reveal whether this technique alone is effective enough to battle and eradicate cancer cells. It is interesting to note that Bi_2S_3@BSA, Bi_2S_3@BSA-Fe_3O_4 and Bi_2S_3@BSA-Fe_3O_4-FA nanoparticles in the absence of X-ray radiation had no significant effects on the survival rate of 4T1 cells, and the same result was also observed in the analysis of cytotoxicity against normal HFF2 cells (Fig. 3b). However, once the nanoparticles are combined with X-ray radiation, significant anti-cancer activity was realized, reinforcing the superiority of the combined therapy over monotherapy. These results further confirm the radiation sensitizing capacity of the prepared nanoparticles against cancer. The cell survival rate for Bi_2S_3@BSA, Bi_2S_3@BSA-Fe_3O_4 and Bi_2S_3@BSA-Fe_3O_4-FA nanoparticles upon X-ray irradiation at 25 mg/mL concentration were 84 %, 78 % and 71 %, respectively. These findings indicate that there is a statistically significant difference between Bi_2S_3@BSA, Bi_2S_3@BSA-Fe_3O_4 and Bi_2S_3@BSA-Fe_3O_4-FA nanoparticles in the presence of X-ray irradiation compared to the absence of irradiation. This can be explained by nanoparticle-triggered ROS production within cells upon X-ray irradiation. The addition of Fe_3O_4 and FA to the Bi_2S_3@BSA structure increased the ROS generation efficiency, intracellular trafficking and targeting capability under X-ray irradiation and led to obvious decline in viability of cells [18,56]. The cell viability declined to 55 % when the cells were treated with Bi_2S_3@BSA-Fe_3O_4-FA (225 mg/mL) along with X-ray. The correlation between cell survival rate and nanoparticle concentration is noteworthy because by increasing the nanoparticle concentration, the cell survival rate dramatically decreases. The nanoparticles exhibited dose-dependent toxicity behavior, where the cell survival rate for Bi_2S_3@BSA, Bi_2S_3@BSA-Fe_3O_4 and Bi_2S_3@BSA-Fe_3O_4-FA nanoparticles upon X-ray irradiation at concentration of 225 mg/mL were 71 %, 64 % and 55 %, respectively (Fig. 3c). The cytotoxicity effect was enhanced for all nanoparticle groups as the concentration increased from 25 mg/mL to 225 mg/mL. These results coincide with the previous findings in the literature that reported significant improvement in radiosensitization of cancer cells using folic acid modified metallic nanoparticles. Magnesium oxide (MgO) nanoparticles decorated with FA and hyaluronic acid (HA) fabricated by Askar et al. for enhanced radiosensitization of breast cancer, showed high selectivity and uptake along with high anticancer activity, which are in line with our findings [57]. Altogether, MTT test results prove that cells are more sensitive to radiation in the presence of nanoparticles, indicating the benefit of radiosensitizers in radiation-induced cancer therapy.

3.3.4. *Cellular uptake and internalization efficacy*

Nanoparticles with no specific targeting motif(s) can be internalized by both cancer and healthy cells, causing toxicity to healthy cells and poor treatment efficacy. Herein, we covalently conjugated FA moieties to the nanoparticles, as folate receptor-mediated endocytosis is considered as a significant uptake mechanism in cancer cells. Accordingly, higher cellular internalization is anticipated for the FA-conjugated particles compared to nonconjugated ones. Both Bi_2S_3@BSA-Fe_3O_4 and Bi_2S_3@BSA-Fe_3O_4-FA nanoparticles with different concentrations were labeled with fluorescein isothiocyanate (FITC) and their cellular uptake was exploited. Intracellular trafficking and targeting capability of Bi_2S_3@BSA-Fe_3O_4 nanoparticles are effectively enhanced by

conjugation of FA on their surface compared to non-targeted nanoparticles (Fig. 3d). Besides, a concentration-dependent cellular uptake behavior was observed as illustrated in Fig. 3d, indicating that FA moieties can facilitate the cellular uptake of nanoparticles, which underlines the importance of targeting moieties in cell internalization [58]. Liu et al. developed Fe_3O_4@C/ZnO nanocomposites decorated with FA for enhanced synergistic tumor therapy. The cellular uptake studies revealed that Fe_3O_4@C/ZnO-FA nanocomposites could be efficiently internalized by HeLa cells due to the presence of FA on the surface of bimetallic nanocomposites, which agrees well with our results [59]. Therefore, to restrict the broad biodistribution of nanoparticles and effectively direct them toward the intended site of actions, conjugation of targeting motifs is required.

3.3.5. *Calcein-AM/PI cell staining assay*

In order to evaluate the potential of nanoparticles to induce cell death, the Calcein-AM/PI cell staining assay was performed. In this method, Calcein-AM and PI solutions are used to stain viable and dead cells, respectively. Accordingly, the potential of the Bi_2S_3@BSA, Bi_2S_3@BSA-Fe_3O_4 and Bi_2S_3@BSA-Fe_3O_4-FA nanoparticles in killing cells upon X-ray irradiation was investigated *via* Calcein AM/PI cell staining assay (Fig. 4a). The increasing intensity of red colored dots in the fluorescence image indicates a higher rate of cell death, whereas the green color represents viable cells. It is clearly depicted that the X-ray irradiation has little effect (little red spots observed) on 4T1 cells without nanoparticle treatment. However, co-treatment of 4T1 cells by X-ray and nanoradiosensitizers resulted in higher cell death. As shown in Fig. 4a, the highest rate of cell death occurred when cells were treated with Bi_2S_3@BSA-Fe_3O_4-FA and X-ray. This is due to the use of high-Z metals such as Bi and Fe in the structure of nanoparticles, which leads to generation of more oxygen-sensitive species in the presence of X-rays irradiation. Higher cell death was observed when high-Z metallic nanoparticles and irradiation were applied together [60]. DNA damage brought on by radiation has typically been seen as the primary factor in mutation and cell death. However, radiation-induced mitochondrial damage is also getting more and more attention [61]. Notably, mitochondria are the only sites where extranuclear DNA resides. Ionizing radiation can induce various lesions in the circular mitochondrial DNA, such as strand breaks, base mismatches, and large deletions, which are also observed in nuclear DNA [61,62]. As a result, in addition to the cell nucleus, mitochondria are expected to be a primary target of ionizing radiation [63].

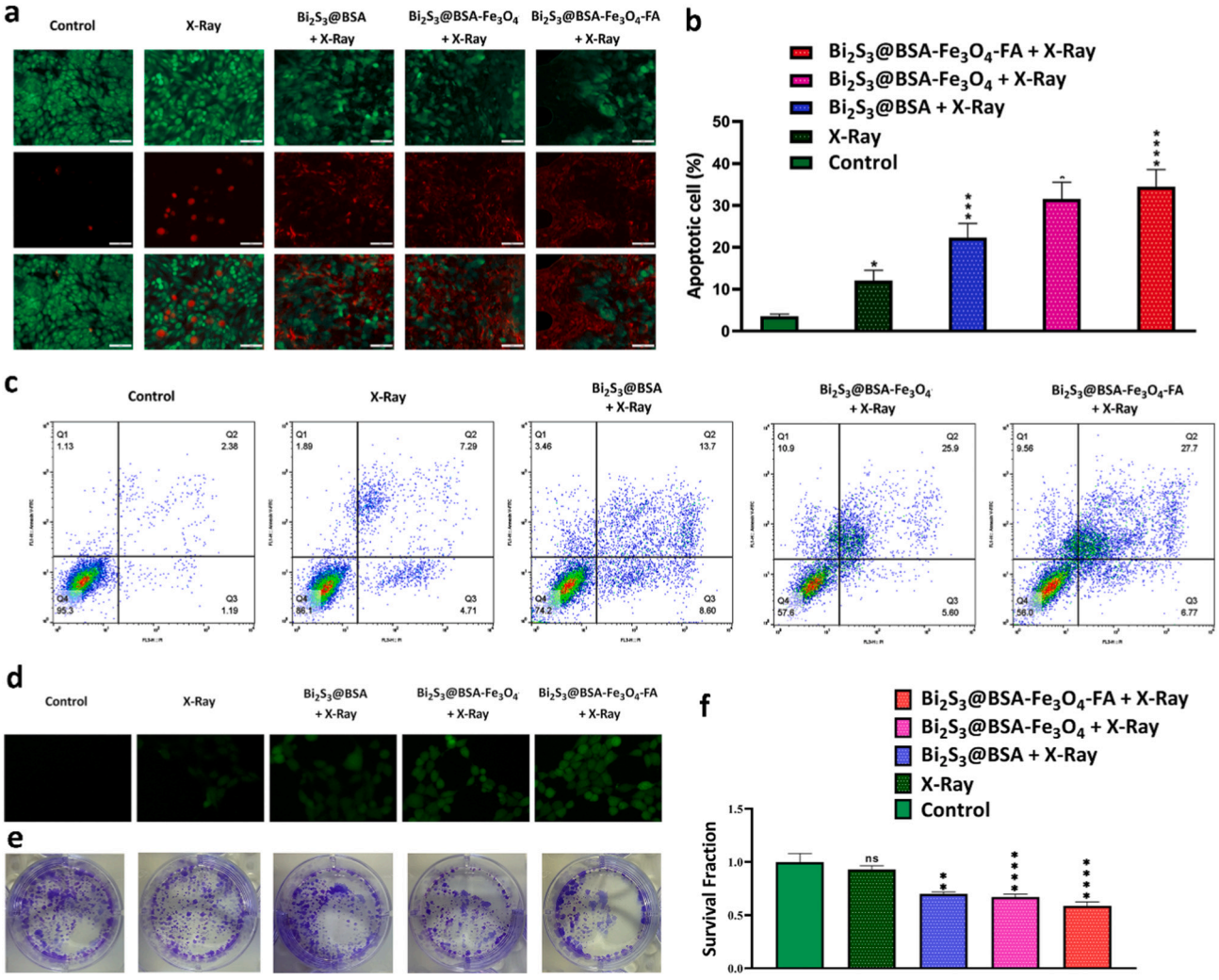

Fig. 4. *In vitro* antitumor activity assays, radiosensitization ability of Bi_2S_3@BSA, Bi_2S_3@BSA-Fe_3O_4 and Bi_2S_3@BSA-Fe_3O_4-FA nanoparticles. (a) Fluorescence images of 4T1 cells after different treatments with calcein-AM/PI staining (the scale bar represents 100 μm); (b& c) Apoptotic analysis of 4T1 cells after different treatments with annexin V-FITC/PI staining and detected by flow cytometry. (d) ROS production of developed nanoparticles upon X-ray irradiation within 4T1 cells after treatment with DCFH-DA; (e) Representative photographs and f) quantitative analysis of colony formation of cells after treatment with different nanoparticles in the presence of X-ray irradiation.

3.3.6. Apoptosis activation

It has been reported that apoptotic cell death often occurs by the induction of DNA damages during radiotherapy of cancer cells. In this case, apoptosis is a favorable process in cancer radiotherapy and may be promoted by some newly developed effective nanoplatforms [64]. Using flow cytometry assay, the apoptotic potential of Bi_2S_3@BSA, Bi_2S_3@BSA-Fe_3O_4 and Bi_2S_3@BSA-Fe_3O_4-FA nanoparticles upon X-ray radiation was investigated under the hypoxia condition, a hallmark of almost all solid malignancy features. As shown in Fig. 4b, apoptotic results clearly indicated that Bi_2S_3@BSA, Bi_2S_3@BSA-Fe_3O_4 and Bi_2S_3@BSA-Fe_3O_4-FA nanoparticles effectively induced cell apoptosis, but the population of cell apoptosis caused by these nanoparticles differ from each other. The potential capability of these nanoparticles to induce cell apoptosis in the presence of X-ray irradiation is as follows: Bi_2S_3@BSA-Fe_3O_4-FA > Bi_2S_3@BSA-Fe_3O_4 > Bi_2S_3@BSA. The rate of both late and early apoptosis in cells treated with Bi_2S_3@BSA, Bi_2S_3@BSA-Fe_3O_4 and Bi_2S_3@BSA-Fe_3O_4-FA nanoparticles were higher compared to the control group. Indeed, the order of induction of late apoptosis by various treatment regimens is as follows: Bi_2S_3@BSA-Fe_3O_4-FA + X-ray > Bi_2S_3@BSA-Fe_3O_4 + X-ray > Bi_2S_3@BSA + X-ray > X-ray > control group. While these findings disclose that X-ray radiation can also induce cell apoptosis, they do not announce that it would be efficient enough to be used alone. In fact, the rate of cell apoptosis *via* this modality was not as much as cell apoptosis when combined with other developed nanoparticles, in particular Bi_2S_3@BSA-Fe_3O_4-FA. Bi_2S_3@BSA nanoparticles administered with X-ray induced higher cell apoptosis in comparison to X-ray alone, indicating the importance of bismuth (Bi) metal in the construction of developed radiosensitizers. Similar findings were obtained for Bi_2S_3@BSA-Fe_3O_4, where it exhibited a higher rate of cell apoptosis compared to Bi_2S_3@BSA due to the presence of Fe as well as Bi. Ultimately, following the addition of FA to Bi_2S_3@BSA-Fe_3O_4 nanoparticles, cell apoptosis increased to the highest level when this nanoformulation was co-administrated with X-ray irradiation. These findings further strengthened our conviction that Bi_2S_3@BSA-Fe_3O_4-FA is a potential nanoradiosensitizer for high-throughput radiotherapy of nearly all solid malignancies characterized by low level of oxygen. The presence of Bi_2S_3 and Fe_3O_4 segments potentiates reactive oxygen species (ROS) production and DNA damage upon X-ray irradiation. Besides, the intracellular trafficking and targeting capability of this system are improved by the addition of FA, consistent with enhancing radio-mediated cell death reported for high-Z-based gold nanostars decorated with FA [65]. Our results emphasize that great programmed cell death can be achieved when Bi_2S_3@BSA-Fe_3O_4-FA nanoparticles are co-administered with X-ray irradiation. Altogether, the utility of Bi_2S_3@BSA-Fe_3O_4-FA nanoparticle as a promising nanoradiosensitizer agent is thus underlined.

3.3.7. Intracellular ROS generation

X-rays lead to ROS production, which improves the efficacy of cancer treatment by radiation-induced DNA damage [66]. Intracellular ROS generation was determined using DCFH-DA, a dye that can be oxidized to emit bright green fluorescence. The control group, which was neither X-ray irradiated nor treated with nanoparticles, showed no green fluorescence, indicating no ROS production (Fig. 4c). Under X-ray radiation alone, green fluorescence was barely detected. The fluorescence intensity enhanced when the cells were co-treated with nanoparticles and then X-ray irradiation. Superior ROS production was observed when X-rays were used in conjunction with Bi_2S_3@BSA, Bi_2S_3@BSA-Fe_3O_4 and Bi_2S_3@BSA-Fe_3O_4-FA nanoparticles. This significant increase in fluorescence intensity reveals the importance of combined therapy in cancer treatment, which is more effective compared to the monotherapy. These findings also suggest that Bi_2S_3@BSA, Bi_2S_3@BSA-Fe_3O_4 and Bi_2S_3@BSA-Fe_3O_4-FA nanoparticles synergistically induce ROS generation under X-ray irradiation, which is also well supported by previous findings [67]. These results further strengthened our conviction that the fabricated nanoparticles can potentially induce ROS generation under X-ray irradiation and are effective radiosensitizers. The following order reflects the radiosensitization potential of the developed nanoparticles upon X-ray irradiation: Bi_2S_3@BSA-Fe_3O_4-FA > Bi_2S_3@BSA-Fe_3O_4 > Bi_2S_3@BSA. Indeed, it can be concluded that high level of ROS production and great radiosensitization effect will be obtained when Bi_2S_3@BSA-Fe_3O_4-FA nanoparticles are applied together with X-ray irradiation due to the presence of high-atomic-number Bi and Fe elements in the structure. On the one hand, Bi_2S_3-based semiconductor nanoparticles are well-known for their promise to enhance the efficacy of radiotherapy by promoting reactive oxygen species (ROS) generation and ultimately DNA double-strand breaks [68–70]. On the other hand, like many other nanomaterials with rich high-Z elements, Fe_3O_4-based nanoparticles induce ROS generation through the catalysis of the Fenton reaction [71]. Yu et al. reported that Fe_5C_2@Fe_3O_4 nanoparticles with high-Z Fe content take advantage of the acidic microenvironment of tumors to liberate ferrous ions to disproportionate H_2O_2 into $^{\bullet}OH$ radicals, leading to the suppression of tumor cells. Moreover, these nanoparticles are favorable for both magnetic targeting and T2-weighted magnetic resonance imaging [71]. Although some nanoparticles, such as porous platinum (Pt) nanoparticles, do not increase the intracellular ROS level when administered alone, it has been reported that when applied in conjunction with radiotherapy, they significantly enhance intracellular ROS generation compared to Pt nanoparticles (33.8 fold) or RT (3.3 fold) administrated alone [67]. Altogether, the combined therapy applied will lead to higher levels of DNA damage and thus improve treatment efficacy.

3.3.8. In vitro colony formation

After demonstrating the efficient cellular uptake, ROS generation, induction of cell apoptosis and good biocompatibility of Bi_2S_3@BSA-Fe_3O_4-FA nanoparticles, *in vitro* cell survival test was carried out by clonogenic assay, which is regarded as a common technique for assessing the cell reproductive death after irradiation [72]. The *in vitro* colony formation in cells treated with different nanoparticles after X-ray irradiation is depicted in Fig. 4d and e. The colony formation was statistically decreased in cells treated with X-ray alone and all of the nanoparticle groups along with X-ray compared to the control group. These results clearly indicate that Bi_2S_3@BSA, Bi_2S_3@BSA-Fe_3O_4 and Bi_2S_3@BSA-Fe_3O_4-FA nanoparticles can effectively induce cell death in varying amounts. The colony formation in cells treated with Bi_2S_3@BSA-Fe_3O_4-FA nanoparticles together with X-ray irradiation markedly decreased compared to other groups (Fig. 4e). This finding provides further evidence for the usefulness of high-Z metals in the construction of nanoradiosensitizers to generate effective ROS products in the presence of X-ray irradiation and, consequently, in restricting the repopulation ability of cancer cells [73]. These promising results were observed not only in clonogenic assay, but also in the cellular uptake, ROS generation, apoptosis, cytotoxicity, and live/dead cell staining (Calcein-AM/PI) with the same *in vitro* treatments, supporting our findings.

3.4. In vivo assays

3.4.1. LD_{50} as an in vivo biosafety indicator

To ensure *in vivo* biosafety of nanoparticles and, consequently, increase their potential in becoming appropriate candidates for preclinical studies, *in vivo* biosafety was exploited. Different doses of nanoparticles were injected intravenously, and the behavior and survival rate of mice were monitored. The results are shown in Cox Regression diagram (Fig. S4). No deaths were recorded at any of the injected doses, and body weight monitoring did not differ significantly from the control group. These tests highlighted that the nanoparticles had no deleterious effects, further strengthening our confidence in the *in vivo* biosafety of Bi_2S_3@BSA-Fe_3O_4-FA nanoparticles for preclinical investigation.

3.4.2. In vivo antitumor activity by enhanced X-ray radiation therapy

In recent years, many efforts have been devoted to radiation therapy

aimed at preferentially sensitizing tumor cells to ionizing radiation while minimizing the deleterious effects on healthy cells [74]. In cancer radiotherapy, enhancing the response of tumor to radiation and improving the therapeutic index by using metallic radiosensitizers have emerged as a promising approach [75]. Recent advances in the development of innovative radiosensitizers along with harnessing the power of nanotechnology have launched a novel treatment modality in cancer radiotherapy. Fascinated by the *in vitro* outcomes such as cellular uptake, ROS generation, apoptosis, cytotoxicity, clonogenic assay and the live/dead cell staining (Calcein-AM/PI), we complementary evaluated the *in vivo* antitumor effects of Bi_2S_3@BSA-Fe_3O_4-FA nanoparticles. This assay was performed once tumors reached a mean volume of ~100 mm^3, then mice were randomly divided into six groups of five mice each. *In vivo* mouse models of breast cancer were then treated with the following regimens: Bi_2S_3@BSA-Fe_3O_4-FA, (2) Bi_2S_3@BSA-Fe_3O_4-FA with 4Gy X-ray, (3) Bi_2S_3@BSA-Fe_3O_4 with 4Gy X-ray, (4) Bi_2S_3@BSA with 4Gy X-ray, (5) PBS and X-ray. The *in vivo* tumor suppression effects of the groups following intravenous injection are shown in Fig. 5a. It was found that implementation of the conventional X-ray dose (4 Gy) alone could not effectively suppress tumor growth. Similar ineffective antitumor activity was observed following intravenous injection of Bi_2S_3@BSA-Fe_3O_4-FA, Bi_2S_3@BSA-Fe_3O_4 and Bi_2S_3@BSA nanoparticles, while once the treatment was combined with X-ray radiation (4 Gy), their effectiveness changed dramatically. Bi_2S_3@BSA-Fe_3O_4-FA nanoparticles with the aid of X-ray radiation can effectively suppress the tumor growth just by a single dose injection. Complete ablation of tumors was observed in three mice out of five within 15 days following a single intravenous injection of Bi_2S_3@BSA-Fe_3O_4-FA nanoparticles combined with X-ray radiation.

This indicates the strong radiosensitization capacity of bimetallic

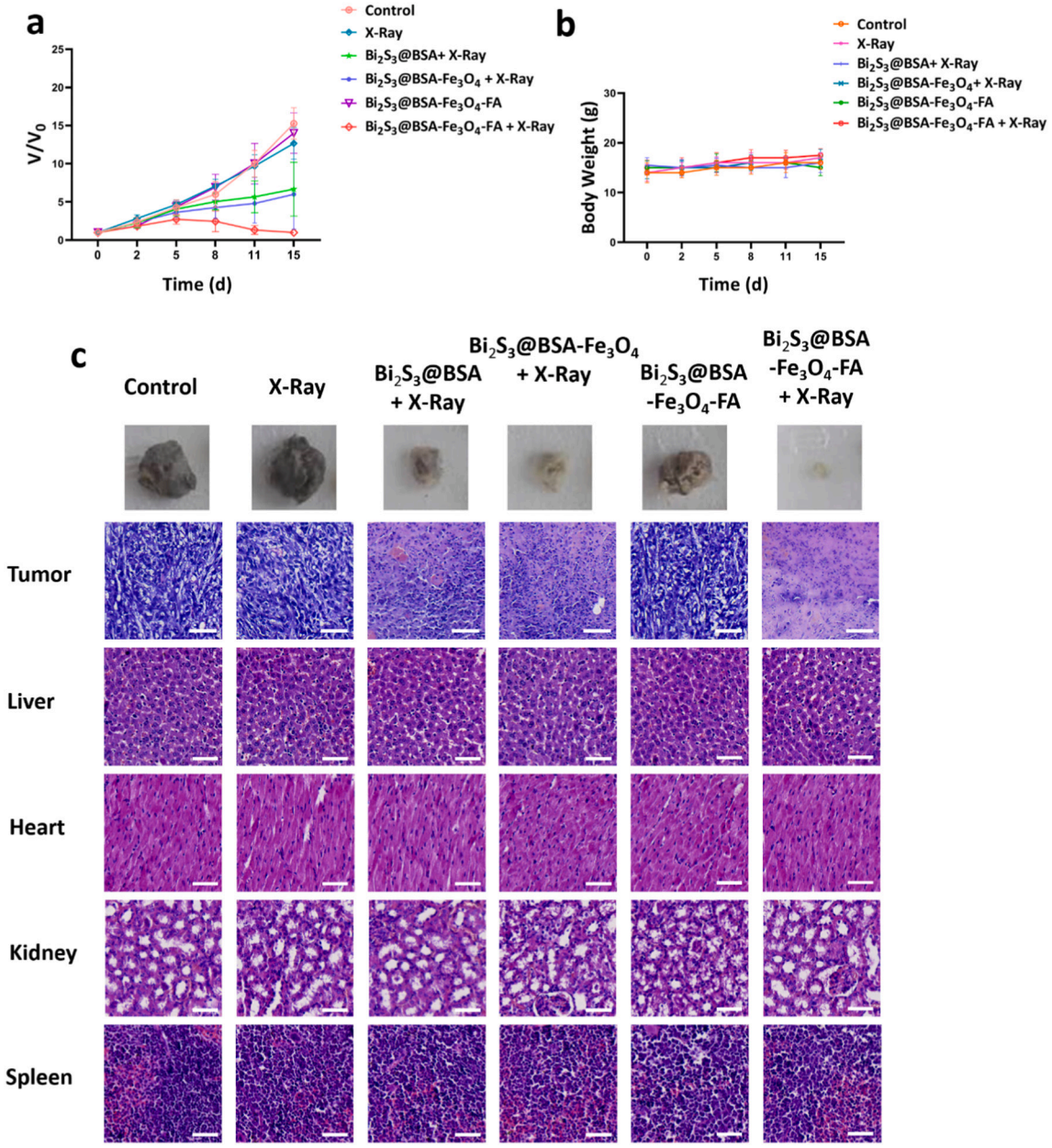

Fig. 5. *In vivo* studies of antitumor effects: (a) Tumor volumes following different treatments with or without X-ray irradiation; (b) Body weight of mice with different treatments (c) Representative tumors' photographs of mice treated with various treatment plans, and H&E staining of the tumor and main organs in the presence and absence of X-ray (Scale bar: 50 μm).

Bi_2S_3@BSA-Fe_3O_4-FA structure, where the generation of ROS upon X-ray irradiation along with great targeting capability owing to the FA has been concluded. FA potentiates the accumulation of bimetallic nano-radiosensitizers within the tumor site, and X-ray irradiation provides the degree of ROS level increase. Our results are in agreement with another study in which high levels of tumor suppression were observed in mice intravenously injected with a biocompatible FA functionalized gold nanorod@polypyrrole@Fe_3O_4 nanoparticles after irradiation [76]. Furthermore, any changes in body weight of mice involved in this assay were precisely monitored over the experimental time periods (Fig. 5b). It is notable that no significant changes in body weight were observed for all experimental groups, which reinforces the usefulness of Bi_2S_3@BSA-Fe_3O_4-FA nanoparticles as a safe radiation sensitizer in cancer radiotherapy.

3.4.3. Histopathology analysis

Pathological hematoxylin & eosin (H&E) images of tumor tissue were analyzed to assess tissue damages in the tumor cells. The results clearly showed that Bi_2S_3@BSA-Fe_3O_4-FA with X-ray irradiation could potentially damage tumor cells, as evidenced by the presence of more necrotic-shaped cells as well as extensive shadow area, which is highly consistent with previous reported data [77]. On the 15th day of the treatment, mice from different groups were euthanized and their major organs such as the kidney, spleen, liver and heart were collected for further analysis. Ultimately, H&E staining was used to reveal whether these nanoparticles can cause any toxicity or not (Fig. 5c). As expected, the groups treated with the nanoparticles showed no obvious abnormalities in the above-mentioned organs compared to the control group, thus reaffirming the safety of Bi_2S_3@BSA-Fe_3O_4-FA.

4. Conclusions

In the current study, a novel bimetallic nanoradiosensitizer with effective tumor-targeting capability, high stability, favorable morphology, and size was developed. The nanoradiosensitizer was designed to provide all essential influencing factors in a single multifunctional nanoplatform for enhanced anticancer efficacy while attenuating adverse effects. Accordingly, the results of both *in vivo* and *in vitro* investigations disclosed that the foregoing objectives are completely reachable by the developed nanoformulation. Fe_3O_4–Bi_2S_3–BSA–FA presented a great capacity in radiosensitization of tumor cells. Exploitation of biological safety revealed that the final formulation did not cause any adverse effects. The biosafety of nanoparticles, along with other exceptional physiochemical properties, can hasten their application to reach into the clinical translation. The most remarkable result is that the implementation of this bimetallic nanocomposite along with X-ray radiation leads to complete ablation of tumors in a murine model *via* radiation-induced DNA damage. Altogether, this versatile nanoplatform offers new insights toward the application of multifunctional high-Z bimetallic nanoradiosensitizers for cancer radiotherapy with synergistic antitumor effects.

Ethical considerations

This study was approved by the Ethics Committee of the Iran National Science Foundation (Code: INSF-98024375), and the study participants signed an informed consent.

Data availability statement

The raw/processed data required to reproduce these findings cannot be shared at this time as the data also forms part of an ongoing study.

CRediT authorship contribution statement

Hamed Nosrati, Mohammadreza Ghaffarlou, Marziyeh Salehiabar, Navid Mousazadeh, Fatemeh Abhari, Murat Barsbay, Yavuz Nuri Ertas, Hamid Rashidzadeh, Ali Mohammadi, Leila Nasehi, Hamed Rezaeejam, Soodabeh Davaran, Ali Ramazani: Investigation. **Hamed Nosrati, João Conde, Hossein Danafar:** Writing - Reviewing and Editing. **João Conde, Hossein Danafar:** Project administration and Funding acquisition.

Declaration of competing interest

J.C. is a co-founder and shareholder of TargTex S.A.

Data availability

The authors do not have permission to share data.

Acknowledgments

This work supported by the “Iran National Science Foundation: INSF-98024375”, Iran's National Elites Foundation, and the “University of Zanjan”. We gratefully acknowledge the Zanjan University of Medical Science support. JC acknowledges financial support from the European Research Council - ERC Starting Grant 848325. Y.N. Ertas acknowledges funding support from the 2232 International Fellowship for Outstanding Researchers Program of TÜBİTAK (Project No: 118C346). MB acknowledges the financial support of the International Atomic Energy Agency (IAEA) under coordinated research project F22070 (IAEA Research Contract No: 23192).

Appendix A. Supplementary data

Supplementary data to this article can be found online at https://doi.org/10.1016/j.bioadv.2022.213090.

References

[1] E.M. Alvarez, L.M. Force, R. Xu, K. Compton, D. Lu, H.J. Henrikson, et al., The global burden of adolescent and young adult cancer in 2019: a systematic analysis for the global burden of disease study 2019, Lancet Oncol. 23 (1) (2022) 27–52.
[2] J.M. Kocarnik, K. Compton, F.E. Dean, W. Fu, B.L. Gaw, J.D. Harvey, et al., Cancer incidence, mortality, years of life lost, years lived with disability, and disability-adjusted life years for 29 cancer groups from 2010 to 2019: a systematic analysis for the Global Burden of Disease Study 2019, JAMA Oncology 8 (2021) 420–444.
[3] K.R. Paulson, A.M. Kamath, T. Alam, K. Bienhoff, G.G. Abady, J. Abbas, et al., Global, regional, and national progress towards Sustainable Development Goal 3.2 for neonatal and child health: all-cause and cause-specific mortality findings from the global burden of disease study 2019, Lancet 398 (10303) (2021) 870–905.
[4] X. Xu, S. Wang, H. Wu, Y. Liu, F. Xu, J. Zhao, A multimodal antimicrobial platform based on MXene for treatment of wound infection, Colloids Surf. B: Biointerfaces 207 (2021), 111979.
[5] S. Wang, Y. Yang, H. Wu, J. Li, P. Xie, F. Xu, et al., Thermosensitive and tum or microenvironment activated nanotheranostics for the chemodynamic/photothermal therapy of colorectal tumor, J. Colloid Interface Sci. 612 (2022) 223–234.
[6] H. Li, W. Xu, F. Li, R. Zeng, X. Zhang, X. Wang, et al., Amplification of anticancer efficacy by co-delivery of doxorubicin and lonidamine with extracellular vesicles, Drug Deliv. 29 (1) (2022) 192–202.
[7] E. Ahmadian, A. Eftekhari, H. Babaei, A.M. Nayebi, M.A. Eghbal, Anti-cancer effects of citalopram on hepatocellular carcinoma cells occur via cytochrome C release and the activation of NF-kB, Anti-Cancer Agents Med.Chem. 17 (11) (2017) 1570–1577.
[8] C. Bilynsky, N. Millot, A.L. Papa, Radiation nanosensitizers in cancer therapy—from preclinical discoveries to the outcomes of early clinical trials, Bioeng.Transl.Med. e10256 (2021).
[9] P.G. Prasanna, K. Rawojc, C. Guha, J.C. Buchsbaum, J.U. Miszczyk, C.N. Coleman, Normal tissue injury induced by photon and proton therapies: gaps and opportunities, Int. J. Radiat. Oncol.* Biol.*Phys. 110 (2021) 1325–1340.
[10] F. Boateng, W. Ngwa, Delivery of nanoparticle-based radiosensitizers for radiotherapy applications, Int. J. Mol. Sci. 21 (1) (2020) 273.
[11] B.B. Mendes, D.P. Sousa, J. Conniot, J. Conde, Nanomedicine-based strategies to target and modulate the tumor microenvironment, Trends Cancer 7 (9) (2021) 847–862.
[12] S. Talebian, T. Rodrigues, J. Das Neves, B. Sarmento, R. Langer, J. Conde, Facts and figures on materials science and nanotechnology progress and investment, ACS Nano 15 (10) (2021) 15940–15952.

[13] E-K Lim T Kim S Paik S Haam Y-M Huh K Lee . Nanomaterials for theranostics: recent advances and future challenges. Nanomater.Neoplasms.913-1101.
[14] S. Farahani, N.R. Alam, S. Haghgoo, A. Shirazi, G. Geraily, E. Gorji, et al., The effect of bismuth nanoparticles in kilovoltage and megavoltage radiation therapy using magnetic resonance imaging polymer gel dosimetry, Radiat. Phys. Chem. 170 (2020), 108573.
[15] J. Xie, L. Gong, S. Zhu, Y. Yong, Z. Gu, Y. Zhao, Emerging strategies of nanomaterial-mediated tumor radiosensitization, Adv. Mater. 31 (3) (2019) 1802244.
[16] L. Zheng, R. Zhu, L. Chen, Q. Fu, J. Li, C. Chen, et al., X-ray sensitive high-Z metal nanocrystals for cancer imaging and therapy, Nano Res. 1–12 (2021).
[17] J. Choi, G. Kim, S.B. Cho, H.-J. Im, Radiosensitizing high-Z metal nanoparticles for enhanced radiotherapy of glioblastoma multiforme, J.Nanobiotechnol. 18 (1) (2020) 1–23.
[18] F. Abhari, J. Charmi, H. Rezaeejam, Z. Karimimoghaddam, H. Nosrati, H. Danafar, et al., Folic acid modified bismuth sulfide and gold heterodimers for enhancing radiosensitization of mice tumors to X-ray radiation, ACS Sustain. Chem. Eng. 8 (13) (2020) 5260–5269.
[19] M.H. Faghfoori, H. Nosrati, H. Rezaeejam, J. Charmi, S. Kaboli, B. Johari, et al., Anticancer effect of X-ray triggered methotrexate conjugated albumin coated bismuth sulfide nanoparticles on SW480 colon cancer cell line, Int. J. Pharm. 582 (2020), 119320.
[20] A. Li, X. Li, X. Yu, W. Li, R. Zhao, X. An, et al., Synergistic thermoradiotherapy based on PEGylated Cu3BiS3 ternary semiconductor nanorods with strong absorption in the second near-infrared window, Biomaterials 112 (2017) 164–175.
[21] F. Mao, L. Wen, C. Sun, S. Zhang, G. Wang, J. Zeng, et al., Ultrasmall biocompatible Bi2Se3 nanodots for multimodal imaging-guided synergistic radiophotothermal therapy against cancer, ACS Nano 10 (12) (2016) 11145–11155.
[22] H. Nosrati, J. Charmi, M. Salehiabar, F. Abhari, H. Danafar, Tumor targeted albumin coated bismuth sulfide nanoparticles (Bi2S3) as radiosensitizers and carriers of curcumin for enhanced chemoradiation therapy, ACS Biomater.Sci.Eng. 5 (9) (2019) 4416–4424.
[23] H. Nosrati, E. Attari, F. Abhari, M. Barsbay, M. Ghaffarlou, N. Mousazadeh, et al., Complete ablation of tumors using synchronous chemoradiation with bimetallic theranostic nanoparticles, Bioact.Mater. 7 (2022) 74–84.
[24] X. Hu, J. Sun, F. Li, R. Li, J. Wu, J. He, et al., Renal-clearable hollow bismuth subcarbonate nanotubes for tumor targeted computed tomography imaging and chemoradiotherapy, Nano Lett. 18 (2) (2018) 1196–1204.
[25] O. Rabin, J.M. Perez, J. Grimm, G. Wojtkiewicz, R. Weissleder, An X-ray computed tomography imaging agent based on long-circulating bismuth sulphide nanoparticles, Nat. Mater. 5 (2) (2006) 118–122.
[26] Q. Huang, S. Zhang, H. Zhang, Y. Han, H. Liu, F. Ren, et al., Boosting the radiosensitizing and photothermal performance of Cu2–xSe nanocrystals for synergetic radiophotothermal therapy of orthotopic breast cancer, ACS Nano 13 (2) (2019) 1342–1353.
[27] Y. Yong, X. Cheng, T. Bao, M. Zu, L. Yan, W. Yin, et al., Tungsten sulfide quantum dots as multifunctional nanotheranostics for in vivo dual-modal image-guided photothermal/radiotherapy synergistic therapy, ACS Nano 9 (12) (2015) 12451–12463.
[28] W. Fan, B. Yung, P. Huang, X. Chen, Nanotechnology for multimodal synergistic cancer therapy, Chem. Rev. 117 (22) (2017) 13566–13638.
[29] X.-D. Zhang, D. Wu, X. Shen, J. Chen, Y.-M. Sun, P.-X. Liu, et al., Size-dependent radiosensitization of PEG-coated gold nanoparticles for cancer radiation therapy, Biomaterials 33 (27) (2012) 6408–6419.
[30] H. Nosrati, J. Charmi, F. Abhari, E. Attari, S. Bochani, B. Johari, et al., Improved synergic therapeutic effects of chemoradiation therapy with the aid of a co-drug-loaded nano-radiosensitizer under conventional-dose X-ray irradiation, Biomater. Sci. 8 (15) (2020) 4275–4286.
[31] D. Lu, H. Wang, Q. Shen, K.K. Kondamareddy, D. Neena, Highly efficient visible-light-induced photoactivity of magnetically retrievable Fe3O4@ SiO2@ Bi2WO6@ g-C3N4 hierarchical microspheres for the degradation of organic pollutant and production of hydrogen, J. Phys. Chem. Solids 106 (2017) 76–81.
[32] H. Zhu, R. Jiang, J. Li, Y. Fu, S. Jiang, J. Yao, Magnetically recyclable Fe3O4/Bi2S3 microspheres for effective removal of Congo red dye by simultaneous adsorption and photocatalytic regeneration, Sep. Purif. Technol. 179 (2017) 184–193.
[33] N.K. Yetim, N. Aslan, M.M. Koç, Structural and catalytic properties of Fe3O4 doped Bi2S3 novel magnetic nanocomposites: p-nitrophenol case, J.Environ.Chem.Eng. 8 (5) (2020), 104258.
[34] R. Karacam, N.K. Yetim, M.M. Koç, Structural and magnetic investigation of Bi2S3@ Fe3O4 nanocomposites for medical applications, J. Supercond. Nov. Magn. 33 (9) (2020) 2715–2725.
[35] H. Nosrati, F. Seidi, A. Hosseinmirzaei, N. Mousazadeh, A. Mohammadi, M. Ghaffarlou, et al., Prodrug polymeric nanoconjugates encapsulating gold nanoparticles for enhanced X-ray radiation therapy in breast cancer, Adv.Healthc. Mater. 2102321 (2021).
[36] N. Basu, R. Bhattacharya, P. Mukherjee, Protein-mediated autoreduction of gold salts to gold nanoparticles, Biomed. Mater. 3 (3) (2008), 034105.
[37] Y. Zu, Y. Yong, X. Zhang, J. Yu, X. Dong, W. Yin, et al., Protein-directed synthesis of Bi 2 S 3 nanoparticles as an efficient contrast agent for visualizing the gastrointestinal tract, RSC Adv. 7 (28) (2017) 17505–17513.
[38] G. Marverti, C. Marraccini, A. Martello, D. D'Arca, S. Pacifico, R. Guerrini, et al., Folic acid-peptide conjugates combine selective cancer cell internalization with thymidylate synthase dimer interface targeting, J. Med. Chem. 64 (6) (2021) 3204–3221.
[39] H. Tonbul, A. Sahin, E. Tavukcuoglu, G. Ultav, S. Akbas, Y. Aktas, et al., Folic acid decoration of mesoporous silica nanoparticles to increase cellular uptake and cytotoxic activity of doxorubicin in human breast cancer cells, J.Drug Deliv.Sci. Technol. 63 (2021), 102535.
[40] X. Liang, Y. Xie, J. Wu, J. Wang, M. Petković, M. Stepić, et al., Functional titanium dioxide nanoparticle conjugated with phthalocyanine and folic acid as a promising photosensitizer for targeted photodynamic therapy in vitro and in vivo, J. Photochem. Photobiol. B Biol. 215 (2021), 112122.
[41] M. Pooresmaeil, H. Namazi, R. Salehi, Photoluminescent folic acid functionalized biocompatible and stimuli-responsive nanostructured polymer brushes for targeted and controlled delivery of doxorubicin, Eur. Polym. J. 156 (2021), 110610.
[42] A. Radoń, A. Drygała, Ł. Hawełek, D. Łukowiec, Structure and optical properties of Fe3O4 nanoparticles synthesized by co-precipitation method with different organic modifiers, Mater. Charact. 131 (2017) 148–156.
[43] A. Roca, M. Morales, C. Serna, Synthesis of monodispersed magnetite particles from different organometallic precursors, IEEE Trans. Magn. 42 (10) (2006) 3025–3029.
[44] C. Tang, C. Wang, F. Su, C. Zang, Y. Yang, Z. Zong, et al., Controlled synthesis of urchin-like Bi2S3 via hydrothermal method, Solid State Sci. 12 (8) (2010) 1352–1356.
[45] A. Jana, C. Bhattacharya, S. Sinha, J. Datta, Study of the optimal condition for electroplating of Bi 2 S 3 thin films and their photoelectrochemical characteristics, J. Solid State Electrochem. 13 (9) (2009) 1339–1350.
[46] S. Husain, M. Irfansyah, N.H. Haryanti, S. Suryajaya, S. Arjo, A. Maddu, Synthesis and characterization of Fe3O4 magnetic nanoparticles from iron ore, J. Phys. Conf. Ser. 1242 (1) (2019), 012021.
[47] S. Mourdikoudis, R.M. Pallares, N.T. Thanh, Characterization techniques for nanoparticles: comparison and complementarity upon studying nanoparticle properties, Nanoscale 10 (27) (2018) 12871–12934.
[48] X. Li, L. Zhang, G. He, Fe3O4 doped double-shelled hollow carbon spheres with hierarchical pore network for durable high-performance supercapacitor, Carbon 99 (2016) 514–522.
[49] J. Luo, J. Liu, Z. Zeng, C.F. Ng, L. Ma, H. Zhang, et al., Three-dimensional graphene foam supported Fe3O4 lithium battery anodes with long cycle life and high rate capability, Nano Lett. 13 (12) (2013) 6136–6143.
[50] W. Zhang, C. Kong, G. Lu, Super-paramagnetic nano-Fe 3 O 4/graphene for visible-light-driven hydrogen evolution, Chem. Commun. 51 (50) (2015) 10158–10161.
[51] J. Grigas, E. Talik, V. Lazauskas, X-ray photoelectron spectra and electronic structure of Bi2S3 crystals, Phys. Status Solidi (b) 232 (2) (2002) 220–230.
[52] K. Ai, Y. Liu, J. Liu, Q. Yuan, Y. He, L. Lu, Large-scale synthesis of Bi2S3 nanodots as a contrast agent for in vivo X-ray computed tomography imaging, Adv. Mater. 23 (42) (2011) 4886–4891.
[53] T.C. Taucher, I. Hehn, O.T. Hofmann, M. Zharnikov, E. Zojer, Understanding chemical versus electrostatic shifts in X-ray photoelectron spectra of organic self-assembled monolayers, J. Phys. Chem. C 120 (6) (2016) 3428–3437.
[54] I. Greco, N. Molchanova, E. Holmedal, H. Jenssen, B.D. Hummel, J.L. Watts, et al., Correlation between hemolytic activity, cytotoxicity and systemic in vivo toxicity of synthetic antimicrobial peptides, Sci. Rep. 10 (1) (2020) 1–13.
[55] N. Malhotra, J.-S. Lee, R.A.D. Liman, J.M.S. Ruallo, O.B. Villaflores, T.-R. Ger, et al., Potential toxicity of iron oxide magnetic nanoparticles: a review, Molecules 25 (14) (2020) 3159.
[56] J. Chen, S. Klem, A.K. Jones, B. Orr, M.M. Banaszak Holl, Folate-binding protein self-aggregation drives agglomeration of folic acid targeted iron oxide nanoparticles, Bioconjug. Chem. 28 (1) (2017) 81–87.
[57] M.A. Askar, N.M. Thabet, G.S. El-Sayyad, A.I. El-Batal, M. Abd Elkodous, O.E. El Shawi, et al., Dual hyaluronic acid and folic acid targeting pH-sensitive multifunctional 2DG@ DCA@ MgO-nano-core–shell-radiosensitizer for breast cancer therapy, Cancers 13 (21) (2021) 5571.
[58] A. Sathiyaseelan, K. Saravanakumar, P. Manivasagan, M.S. Jeong, E.-S. Jang, M.-H. Wang, Folic acid conjugated chitosan encapsulated palladium nanoclusters for NIR triggered photothermal breast cancer treatment, Carbohydr. Polym. 119021 (2021).
[59] X. Liu, C. Wang, X. Wang, C. Tian, Y. Shen, M. Zhu, A dual-targeting Fe3O4@ C/ZnO-DOX-FA nanoplatform with pH-responsive drug release and synergetic chemo-photothermal antitumor in vitro and in vivo, Mater. Sci. Eng. C 118 (2021), 111455.
[60] H. Zhu, X. Cao, X. Cai, Y. Tian, D. Wang, J. Qi, et al., Pifithrin-μ incorporated in gold nanoparticle amplifies pro-apoptotic unfolded protein response cascades to potentiate synergistic glioblastoma therapy, Biomaterials 232 (2020), 119677.
[61] W.W.-Y. Kam, R.B. Banati, Effects of ionizing radiation on mitochondria, Free Radic. Biol. Med. 65 (2013) 607–619.
[62] X. Jin, F. Li, B. Liu, X. Zheng, H. Li, F. Ye, et al., Different mitochondrial fragmentation after irradiation with X-rays and carbon ions in HeLa cells and its influence on cellular apoptosis, Biochem. Biophys. Res. Commun. 500 (4) (2018) 958–965.
[63] Y. Chen, N. Li, J. Wang, X. Zhang, W. Pan, L. Yu, et al., Enhancement of mitochondrial ROS accumulation and radiotherapeutic efficacy using a Gd-doped titania nanosensitizer, Theranostics 9 (1) (2019) 167–178.
[64] S. Elmore, Apoptosis: a review of programmed cell death, Toxicol. Pathol. 35 (4) (2007) 495–516.
[65] P. Hu, X. Hou, X. Yu, X. Wei, Y. Li, D. Yang, et al., Folic acid-conjugated gold nanostars for computed tomography imaging and photothermal/radiation combined therapy, ACS Appl.Bio Mater. 4 (2021) 4862–4871.
[66] K. Ni, G. Lan, W. Lin, Nanoscale metal–organic frameworks generate reactive oxygen species for cancer therapy, ACS Cent.Sci. 6 (6) (2020) 861–868.
[67] Y. Li, K.-H. Yun, H. Lee, S.-H. Goh, Y.-G. Suh, Y. Choi, Porous platinum nanoparticles as a high-Z and oxygen generating nanozyme for enhanced radiotherapy in vivo, Biomaterials 197 (2019) 12–19.

[68] Z. Guo, S. Zhu, Y. Yong, X. Zhang, X. Dong, J. Du, et al., Synthesis of BSA-coated BiOI@ Bi2S3 semiconductor heterojunction nanoparticles and their applications for radio/photodynamic/photothermal synergistic therapy of tumor, Adv. Mater. 29 (44) (2017) 1704136.
[69] X. Wang, C. Zhang, J. Du, X. Dong, S. Jian, L. Yan, et al., Enhanced generation of non-oxygen dependent free radicals by schottky-type heterostructures of Au–Bi2S3 nanoparticles via X-ray-induced catalytic reaction for radiosensitization, ACS Nano 13 (5) (2019) 5947–5958.
[70] H. Nosrati, E. Attari, F. Abhari, M. Barsbay, M. Ghaffarlou, N. Mousazadeh, et al., Complete ablation of tumors using synchronous chemoradiation with bimetallic theranostic nanoparticles, Bioact.Mater. 7 (2021) 74–84.
[71] J. Yu, F. Zhao, W. Gao, X. Yang, Y. Ju, L. Zhao, et al., Magnetic reactive oxygen species nanoreactor for switchable magnetic resonance imaging guided cancer therapy based on pH-sensitive Fe5C2@ Fe3O4 nanoparticles, ACS Nano 13 (9) (2019) 10002–10014.
[72] N.A. Franken, H.M. Rodermond, J. Stap, J. Haveman, C. Van Bree, Clonogenic assay of cells in vitro, Nat. Protoc. 1 (5) (2006) 2315–2319.
[73] X. Dong, R. Cheng, S. Zhu, H. Liu, R. Zhou, C. Zhang, et al., A heterojunction structured WO2. 9-WSe2 nanoradiosensitizer increases local tumor ablation and checkpoint blockade immunotherapy upon low radiation dose, ACS Nano 14 (5) (2020) 5400–5416.
[74] E.J. Moding, M.B. Kastan, D.G. Kirsch, Strategies for optimizing the response of cancer and normal tissues to radiation, Nat. Rev. Drug Discov. 12 (7) (2013) 526–542.
[75] F. Moradi, K.R.E. Saraee, S.A. Sani, D. Bradley, Metallic nanoparticle radiosensitization: the role of Monte Carlo simulations towards progress, Radiat. Phys. Chem. 180 (2021), 109294.
[76] W. Cao, X. Wang, L. Song, P. Wang, X. Hou, H. Zhang, et al., Folic acid-conjugated gold nanorod@ polypyrrole@ Fe 3 O 4 nanocomposites for targeted MR/CT/PA multimodal imaging and chemo-photothermal therapy, RSC Adv. 9 (33) (2019) 18874–18887.
[77] H. Nosrati, Y. Baghdadchi, R. Abbasi, M. Barsbay, M. Ghaffarlou, F. Abhari, et al., Iron oxide and gold bimetallic radiosensitizers for synchronous tumor chemoradiation therapy in 4T1 breast cancer murine model, J. Mater. Chem. B 9 (2021) 4510–4522.